ELECTRONIC SUPPLEMENTARY INFORMATION

Ferrocenyl-substituted nitronyl nitroxide in the design of one-dimensional magnets

Kseniya Maryunina,*[a,b] Daria Nigomedyanova,[a,b] Vitaly Morozov,[a] Kristina Smirnova,[a,b] Gleb Letyagin,[a,b] Galina Romanenko,[a,] Nikolay Efimov,[c] Artem Bogomyakov,*[a,b] and Victor Ovcharenko[a]

E-mail: mks@tomo.nsc.ru (K.M.), bus@tomo.nsc.ru (A.B.)

[a] International Tomography Center, SB RAS, Novosibirsk, Russia
[b] Novosibirsk State University, Novosibirsk, Russia
[c] N.S. Kurnakov Institute of General and Inorganic Chemistry, Russian Academy of Sciences, Moscow, Russia

Content

1. Crystal data and experimental details for complexes

Table S1. Crystal data and experimental details for complexes, where L = (Cp)Fe(CpNN), L* = (Cp)Fe(CpIN)$_{0.5}$(CpNN)$_{0.5}$, H$_2$L'$^+$ = CpFe(CpImOH)$^+$

Compound	[Mn(hfac)$_2$L]$_n$	[Co(hfac)$_2$L]$_n$	{L[Co(hfac)$_2$]$_2$L*}	(H$_2$L')[Co(hfac)$_3$]	{[Cu(hfac)$_2$]$_3$L$_2$}	[Zn(hfac)$_2$L]	[Zn(hfac)$_2$L]·0.25C$_6$H$_{14}$
Formula	C$_{27}$H$_{23}$F$_{12}$FeMnN$_2$O$_6$	C$_{27}$H$_{23}$F$_{12}$FeCoN$_2$O$_6$	C$_{54}$H$_{46}$Co$_2$F$_{24}$Fe$_2$N$_4$O$_{11}$	C$_{32}$H$_{26}$CoF$_{18}$FeN$_2$O$_7$	C$_{64}$H$_{48}$Cu$_3$F$_{36}$Fe$_2$N$_4$O$_{16}$	C$_{27}$H$_{23}$F$_{12}$FeZnN$_2$O$_6$	C$_{28.5}$H$_{26.5}$F$_{12}$FeN$_2$O$_6$Zn
FW	810.26	814.25	1612.51	1007.33	2115.38	820.69	842.24
T, K	296	296	296	296	296	296	296
Space group, Z	P2$_1$/n, 4	P2$_1$/n, 4	Pbcn, 4	P2$_1$/c, 4	P-1, 1	P-1, 4	P-1, 4
a, b, c, Å	14.3528(3) 15.6852(4) 14.5169(3)	14.2966(11) 15.5154(13) 14.4767(12)	13.6953(13) 21.185(2) 21.563(2)	15.3968(19) 11.6830(10) 22.175(3)	12.2065(12) 12.3811(12) 14.0205(13)	12.3105(6) 15.4830(8) 19.1434(10)	12.2352(11) 15.0010(14) 21.498(2)
α, β, γ, °	97.424(2)	96.601(5)	90 90 90	90 97.779(9) 90	86.613(5) 71.390(5) 83.519(6)	75.379(3) 87.408(3) 69.457(3)	72.553(4) 89.059(5) 76.936(5)
V, Å^3	3240.74(13)	3189.9(5)	6256.2(11)	3952.2(7)	1994.7(3)	3302.3(3)	3661.1(6)
D$_c$, g cm^{-3}	1.661	1.695	1.713	1.693	1.761	1.651	1.528
θ$_{max}$, deg.	28.296	28.314	67.956	25.350	29.602	28.723	67.922
I$_{hkl}$ (meas/uniq) / R$_{int}$	32946 / 7920 0.0814	31466 / 7926 0.1040	37249 / 5655 / 0.1019	39717 / 7239 / 0.1702	38678 / 10991 / 0.0550	56995 / 16786 / 0.0760	35506/ 12953 / 0.0557
GooF	0.821	0.790	0.932	0.661	0.817	0.823	1.005
I$_{hkl}$(I>2σ$_I$) / Ns	3628 / 523	3054 / 479	4066 / 599	2278 / 663	4993 / 715	7403 / 1054	7674 / 937
R$_1$ / wR$_2$ (I>2σ$_I$)	0.0443 / 0.0790	0.0502 / 0.0739	0.0408 / 0.0999	0.0401 / 0.0451	0.0403 / 0.0895	0.0411 / 0.0885	0.0652 / 0.181
CCDC	2298179	2298176	2298180	2308668	2298178	2298181	2298177

2. Selected bond lengths and angles

Table S2. Selected bond lengths (Å) and angles (deg) in discussed compounds, where L = (Cp)Fe(CpNN), L* = (Cp)Fe(CpIN)$_{0.5}$(CpNN)$_{0.5}$, H$_2$L'$^+$ = CpFe(CpImOH)$^+$

Compound		M–O$_{NO}$	M–O$_{hfac}$	∠MO$_{NO}$N	Fe–C$_{Cp}$	N–O	∠O$_{NO}$MO$_{NO}$	∠Cp–NN	∠hfac–hfac	∠Cp–hfac	Cp…hfac centroids
[Mn(hfac)$_2$L]$_n$		2.171(2)–2.176(2)	2.127(2)–2.156(2)	135.5(1)-136.5(1)	1.982(5)–2.045(3)	1.297(2)–1.292(2)	164.87(7)	2.2	16.3	–	–
[Co(hfac)$_2$L]$_n$		2.123(2)–2.169(2)	2.034(2)–2.072(2)	132.5(2)-135.5(2)	1.977(8)–2.052(4)	1.296(3)–1.290(3)	167.31(8)	1.2	13.9	–	–
{[Cu(hfac)$_2$]$_3$L$_2$}	CuO$_6$	2.666(2)	1.915(2)–1.993(2) 2.201(2)	152.4(1)	2.009(4)–2.034(4)	1.267(2)–	180.00	24.0	180	–	–
	CuO$_5$	1.942 (2)		120.5(1)		1.308(2)	–		85.9	16.8	3.49
[Zn(hfac)$_2$L]	Zn1	1.986(2)	1.989(2)–2.071(2)	117.8(1),	2.014(4)–2.055(3)	1.323(3)–1.264(3)	–	17.7	54.5	13.5	3.52
	Zn2	1.976(2)		118.6(1)		1.320(3)–1.264(3)		28.4	53.5	18.1	3.63
[Zn(hfac)$_2$L] ·0.25C$_6$H$_{14}$	Zn1	1.969(4)	1.987(4)–2.067(4)	117.8(3),	2.013(6)–2.059(6)	1.334(5)–1.261(6)	–	23.4,	49.5	17.8	3.67
	Zn2	1.981(4)		120.8(3)		1.329(5)–1.269(5)		22.5	56.9	21.2	3.66
{L[Co(hfac)$_2$]$_2$L*}		2.095(2)–2.184(2)	2.048(2)–2.084(2)	119.9(1), 134.9(1)	1.98(2)–2.058(4)	1.349(2)–1.301(5)	–	19.1	89.1	–	–
(H$_2$L')[Co(hfac)$_3$]		–	2.052(3)–2.081(3)	–	2.004(5)–2.046(5)	1.368(4)	–	11.2	–	–	–

3. Ferrocenyl-substituted nitronyl nitroxide L, their reduced derivatives L*, H$_2$L'$^+$ and nitronyl ketone L^d
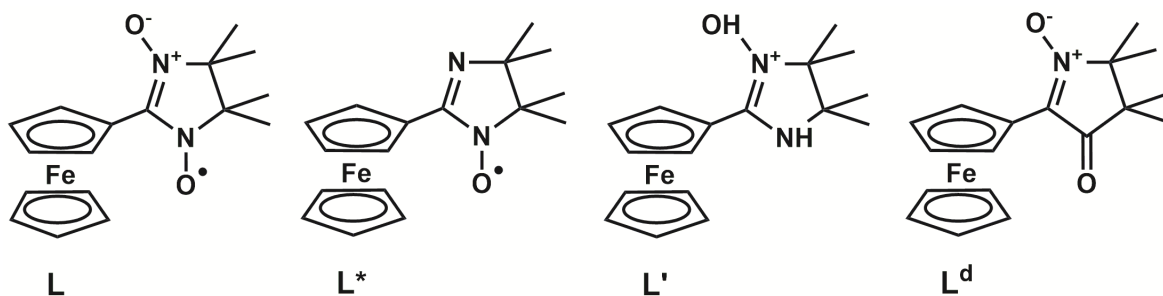
Scheme S1. Ferrocenyl-substituted nitronyl nitroxide L, its reduced derivatives imino nitroxide L* and hydroxy-imidazolinium cation H$_2$L'$^+$, and model diamagnetic analog nitronyl ketone L^d.
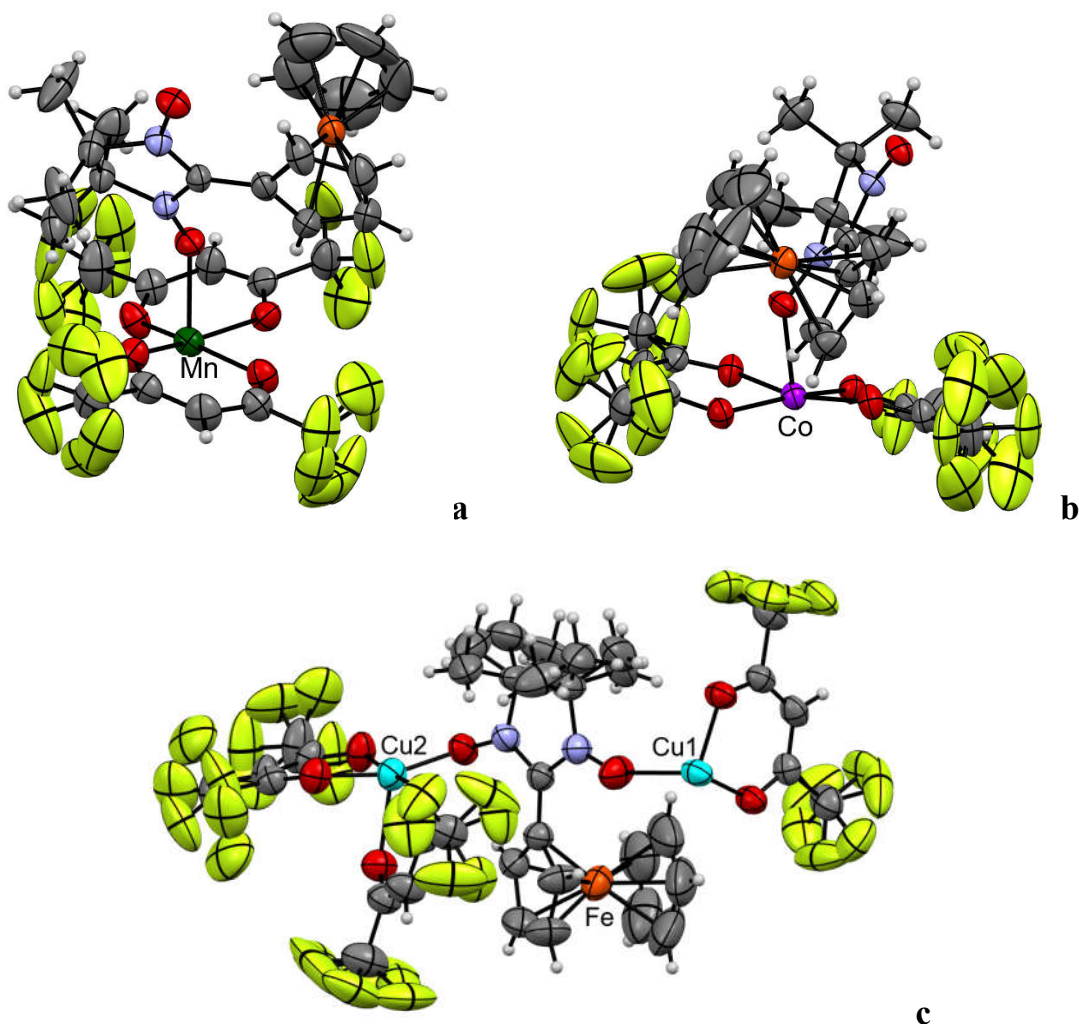
4. Fragments of crystal structures

Figure S1-1. Crystallographically independent parts of chains [Mn(hfac)$_2$L]$_n$ (a), [Co(hfac)$_2$L]$_n$ (b) and molecule {[Cu(hfac)$_2$]$_3$L$_2$} (c). *Colour legend:* N – blue, O – red, H – white, C – grey, F – green, Cu – cyan, Fe – dark orange, Mn – green, Co – violet. Principle ellipsoids for non-hydrogen atoms are given with 50% probability level.
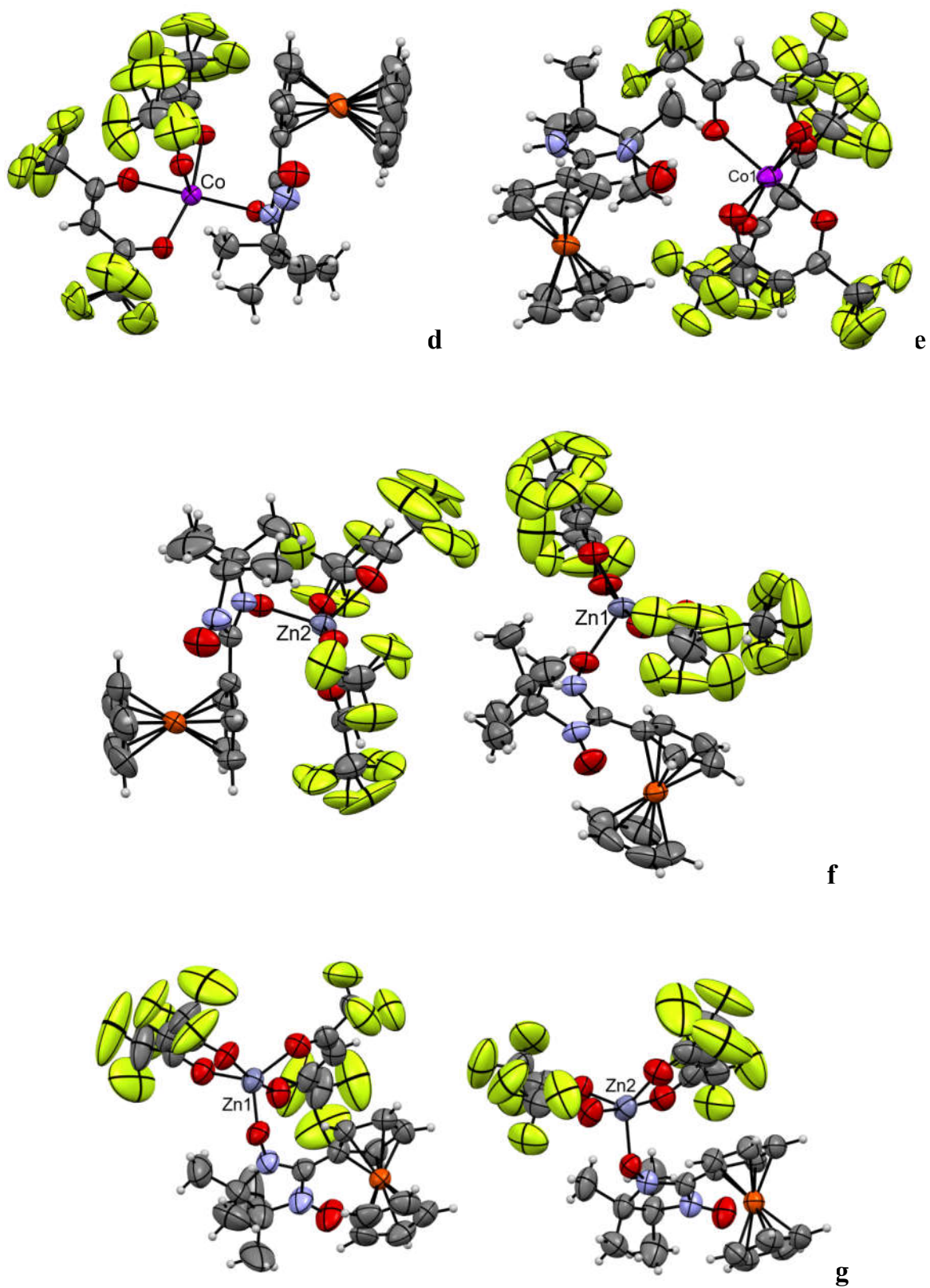
Figure S1-2. Crystallographically independent parts of {L[Co(hfac)$_2$]$_2$L*} (d) and H$_2$L'[Co(hfac)$_3$] (e), structure of molecules in [Zn(hfac)$_2$L] (f) and [Zn(hfac)$_2$L]·0.25C$_6$H$_{14}$ (g). *Colour legend:* N – blue, O – red, H – white, C – grey, F – green, Fe – dark orange, Co – violet, Zn – smoky. Principle ellipsoids for non-hydrogen atoms are given with 50% probability level.

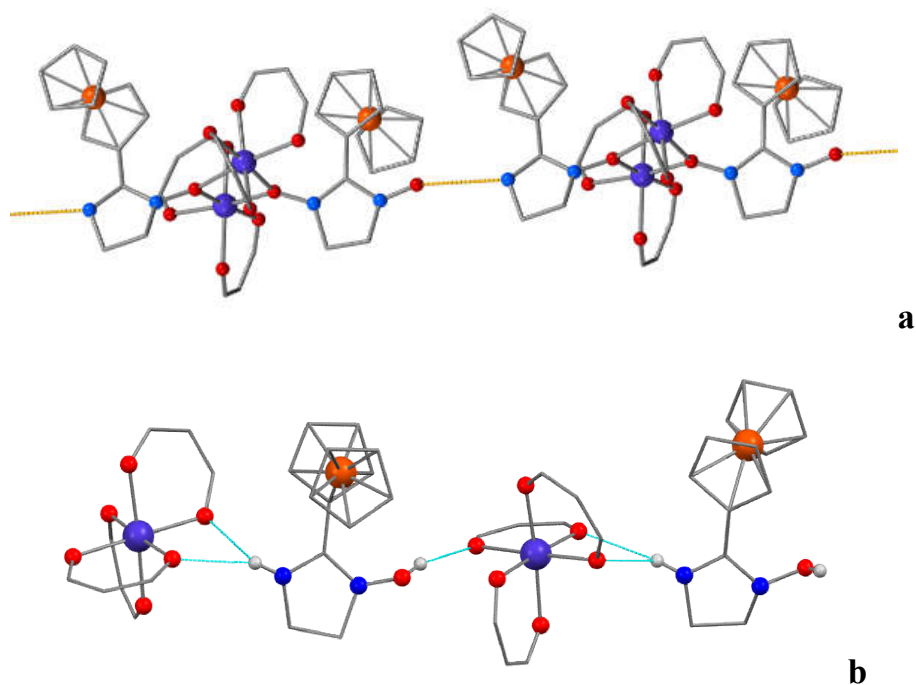## 5. Crystal structure of binuclear {L[Co(hfac)$_2$]$_2$L*} and complex salt H$_2$L'[Co(hfac)$_3$]

Figure S2. Short intermolecular contacts in crystal structures of {L[Co(hfac)$_2$]$_2$L*} (a) and H$_2$L'[Co(hfac)$_3$] (b). *Colour legend:* N – blue, O – red, Fe – dark orange, Co – violet, carbon skeleton – grey; H atoms, CH$_3$- and CF$_3$-groups are omitted for clarity; short contacts O$_{NO}$...N in {L[Co(hfac)$_2$]$_2$L*} are highlighted in yellow (a), H-bonds in H$_2$L'[Co(hfac)$_3$] are coloured in cyan (b).

In the reaction of L with Co(hfac)$_2 \cdot x$H$_2$O along with the chain-polymer complex [Co(hfac)$_2$L]$_n$, the formation of binuclear {L[Co(hfac)$_2$]$_2$L*} and complex salt H$_2$L'[Co(hfac)$_3$] were observed (Fig. S2).

According to SC XRD data, the molecule of the binuclear {L[Co(hfac)$_2$]$_2$L*} complex is centrosymmetric and in the crystal structure the superposition of nitronyl and imino nitroxides is observed (Fig. S2a). Uncoordinated O$_{NO}$ atom of the paramagnetic ligand occupies the position with the weight ½ in the centrosymmetric molecule. In {L[Co(hfac)$_2$]$_2$L*} two O$_{NO}$ atoms of the paramagnetic ligands L and L* act as bridges, linking two Co(hfac)$_2$ fragments with *cis*-coordinated hfac ligands. In this case, the Co-O$_{NO}$ bonds and corresponding $\angle$CoO$_{NO}$N angles are different (2.095(2) and 2.184(2) Å and 119.9(1) and 134.9(1)°, respectively). The N-O$_{Co}$ bond length is equal to 1.349(2) Å and is typical for this kind of bridging coordination of the nitroxide group (average 1.35(2) Å).[1] Nitronyl nitroxide fragment and the associated Cp ring in the paramagnetic ligands are non-coplanar; their planes are rotated at an angle of 19.1°. There are some short O$_{NO} \cdots$N contacts between neighboring molecules of the complexes (3.172(5) Å).

Co-O distances in the [Co(hfac)$_3$]$^-$ complex anion of H$_2$L'[Co(hfac)$_3$] consist of 2.052(3)-2.081(3) Å are indicative of Co^{2+} charge state. Thus, ferrocenyl derivative remains in

its protonated state $H_2L'^+$. Fe-C_{CP} distances in $H_2L'^+$ are typical for the discussed series of compounds (Table S2). While N-O bond length in $H_2L'^+$ (1.368(4) Å) is substantially longer than the one in nitronyl nitroxide L (~1.32 Å). It should be noted, that NOH-group in $H_2L'^+$ is remarkably out of $\{CN_2\}$ plane, which is common for diamagnetic hydroxylamines. Bond lengths C-N are nearly equal (1.317(5)-1.328(6)) in the $\{CN_2O\}$ fragment due to conjugation effect. Hydrogen atoms of $H_2L'^+$ form hydrogen bonds to O_{hfac} atoms linking ions into ribbons (Fig. S2b).
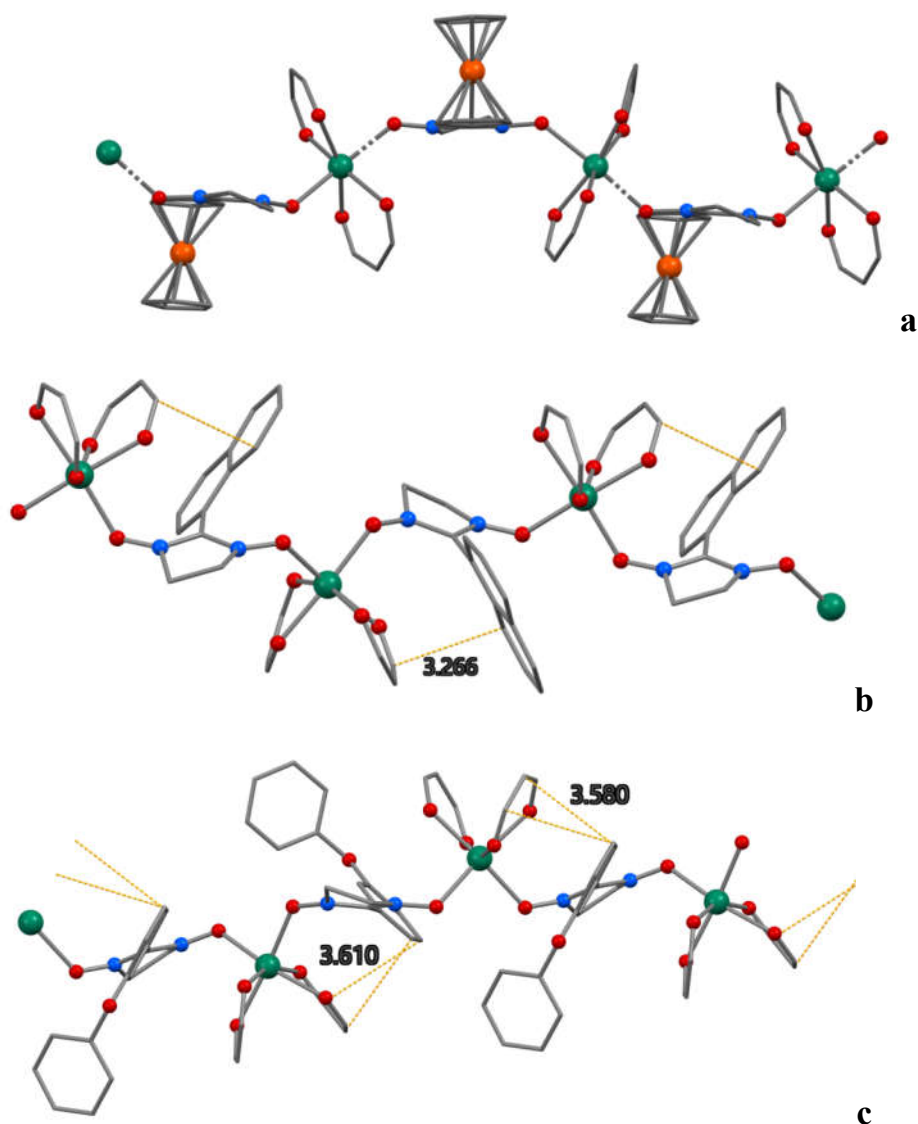
6. Comparison of *trans*- and *cis*-chains

Figure S3. Fragments of chains in *trans*-[Mn(hfac)$_2$L]$_n$ (a), *cis*-[Mn(hfac)$_2$(NN-Naph)]$_n$ (b),[2] and *cis*-[Mn(hfac)$_2$(NN-Ph3OPh)]$_n$ (c).[3] *Colour legend:* N – blue, O – red, Fe – dark orange, Mn – green, carbon skeleton – grey; H atoms, CH$_3$- and CF$_3$-groups are omitted for clarity; intrachain contacts C···C are shown in yellow.

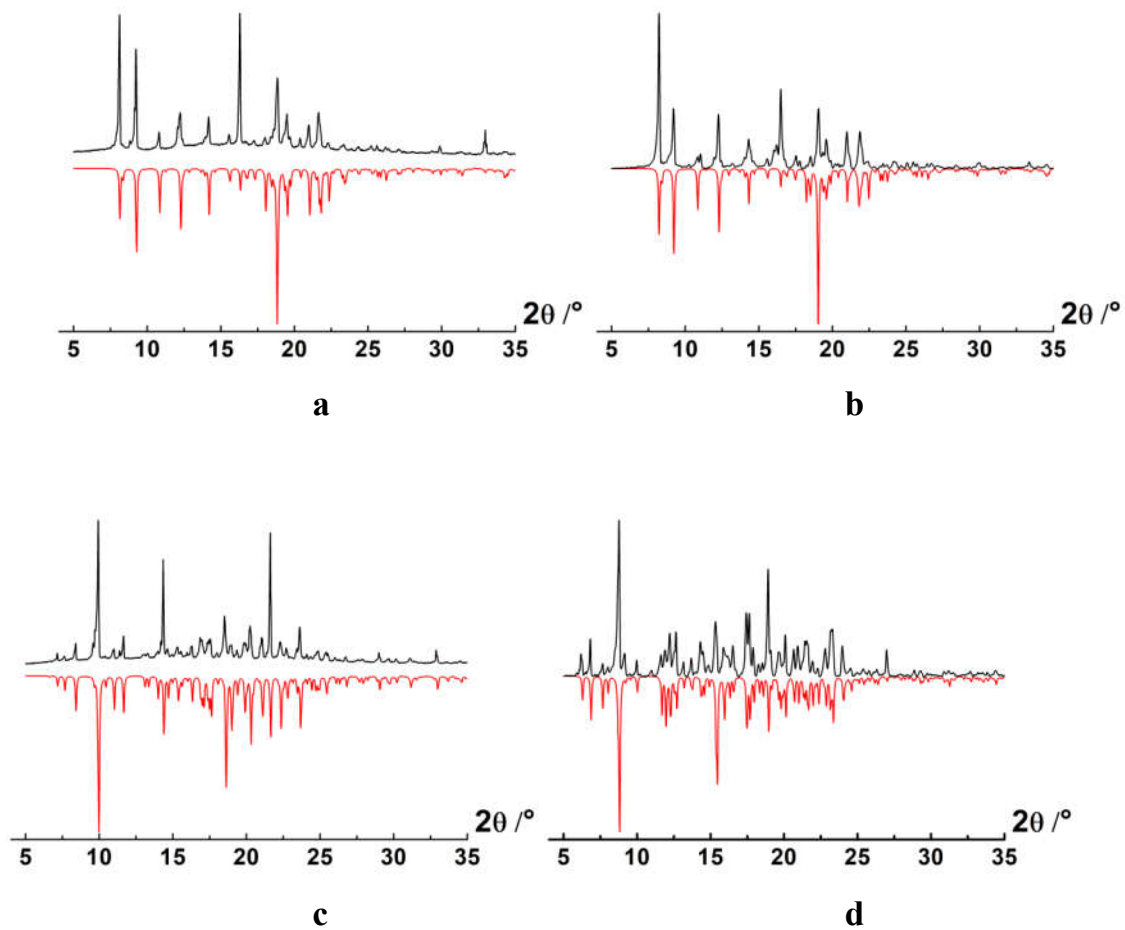# 7. Powder X-ray Diffraction patterns

Figure S4. Comparison of the experimental powder diffraction pattern (black lines) with that simulated from the single crystal structure (red lines) of $[Mn(hfac)_2L]_n$ (a), $[Co(hfac)_2L]_n$ (b), $\{[Cu(hfac)_2]_3L_2\}$ (c), and $[Zn(hfac)_2L]$ (d) at 296 K.

8. Magnetic susceptibility measurements

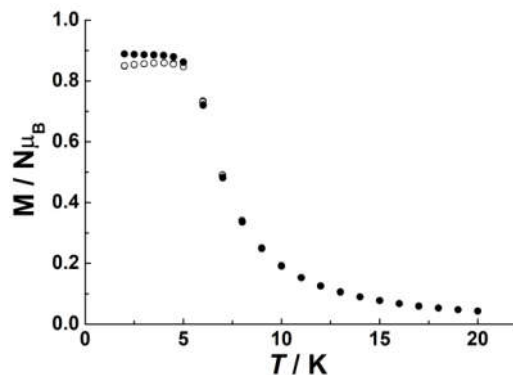**Figure S5.** Zero field cooled (○) and field cooled (●) magnetization at 150 Oe for $[Mn(hfac)_2L]_n$ complex.

a

b

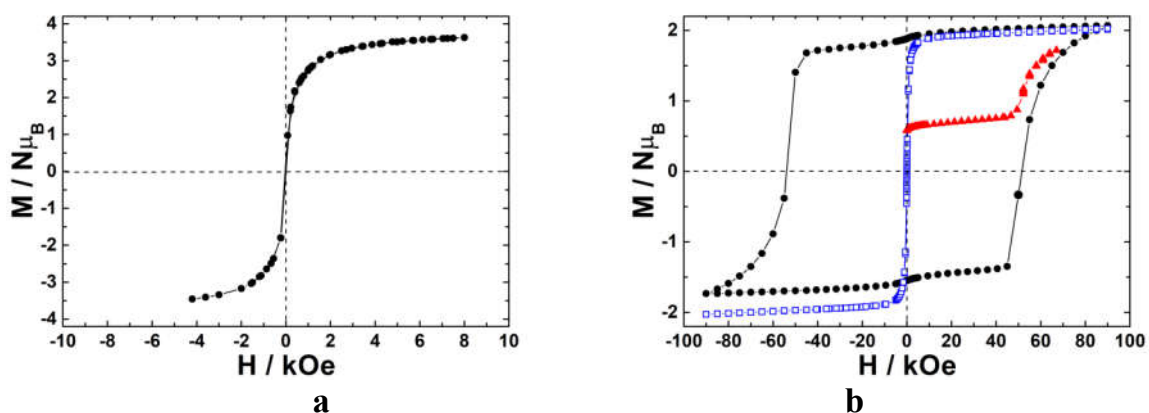**Figure S6.** Field dependences of magnetization for $[Mn(hfac)_2L]_n$ (a: -●- at 2 K, solid line only guide) and for $[Co(hfac)_2L]_n$ (b: -▲- initial magnetization curve from 0 to 67.0 kOe at 2 K, -●- hysteresis loop from -90.0 to 90.0 kOe at 2 K, and -□- magnetization curve from -90.0 to 90.0 kOe at 20 K; solid lines only guide).

In the case of the chain-polymer complex $[Mn(hfac)_2L]_n$, there is no hysteresis in the field dependences of the magnetization curves, and the initial magnetization curve coincides with the subsequent ones (Fig. 6a, black circles). The magnetization of $[Co(hfac)_2L]_n$ at 2 K increases stepwise to ~0.65 $N\mu_B$ in the low magnetic field region, then gradually increases to ~ 0.77 $N\mu_B$ when the magnetic field is increased to 45 kOe. Above 45 kOe, the magnetization increases more sharply (Fig. 6b, red triangles), but saturation cannot be achieved on MPMSXL and PPMS systems H^{max}_{MPMS} = 70 kOe and H^{max}_{PPMS} = 90 kOe). Therefore, hysteresis curves were measured on the PPMS device (Fig. 6b, black circles) by achieving full saturation of ~ 2.0 $N\mu B$ at 20 K (Fig. 6b, empty blue squares) and then lowering the temperature to 2 K while maintaining the field value at 90 kOe.
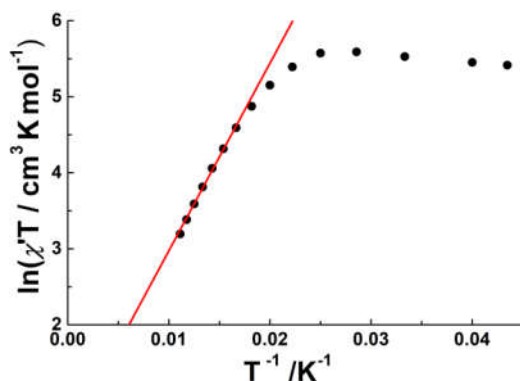
Figure S7. ln($\chi'T$) *vs.* $1/T$ for $[Co(hfac)_2L]_n$ under zero DC field (solid red line corresponds to a linear fitting).

For Ising one-dimensional ordered spin systems, the value of $\chi'T$, where χ' is the real part of the magnetic susceptibility, increases exponentially as the temperature decreases, according to the expression $\chi'T = C_{eff} \cdot exp[\Delta_\xi/(k_B \cdot T)]$, where C_{eff} is the effective Curie constant of the repeating fragment ($C_{eff} = 1$ for $S_{eff} = 1$), and Δ_ξ is the energy required to create a domain wall within the chain, reflecting the degree of correlation between spins.[4] The susceptibility was measured in a magnetic field with amplitude of 3.5 Oe, oscillating at a frequency of 1.0 Hz, in the absence of DC magnetic field in the temperature range of 2-90 K. The linear dependence of ln($\chi'T$) in coordinates ln($\chi'T$) *vs.* $1/T$ in the range of 60-90 K confirms the one-dimensional ordering in $[Co(hfac)_2L]_n$, and the optimal parameters for the linear approximation of the data were: Δ_ξ = 171(4) cm^{-1}, C_{eff} = 1.66(14) cm$^3 \cdot$K$\cdot$mol^{-1}. At temperatures below 40 K, the curve saturates, which is characteristic of the presence of defects (finite-size effect). The strong correlation between spins in the chain suggests that $[Co(hfac)_2L]_n$ is a single-chain magnet with a high energy barrier for magnetization reversal.

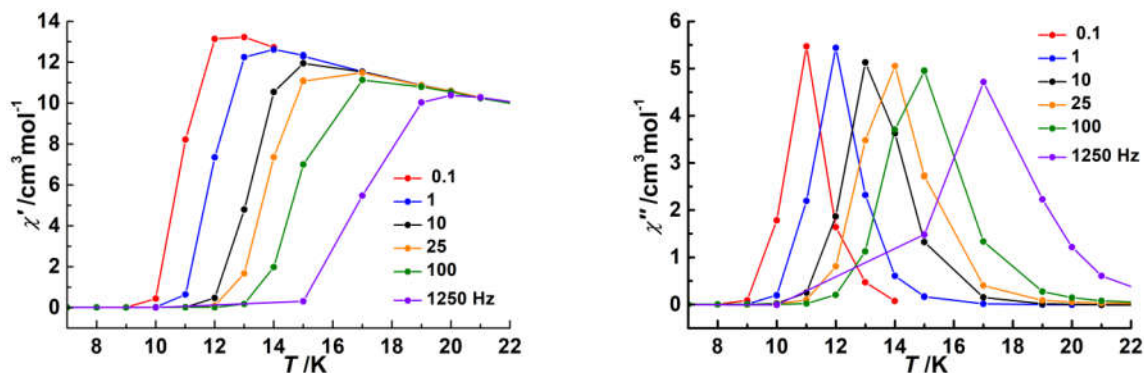**Figure S8.** Temperature dependencies of χ' (in-phase) and χ'' (out-of-phase) components of the AC magnetic susceptibility for $[Co(hfac)_2L]_n$ (under zero DC field with the ac field of 3.5 Oe and the frequency varies in range 0.01–1488 Hz; solid lines only guide).
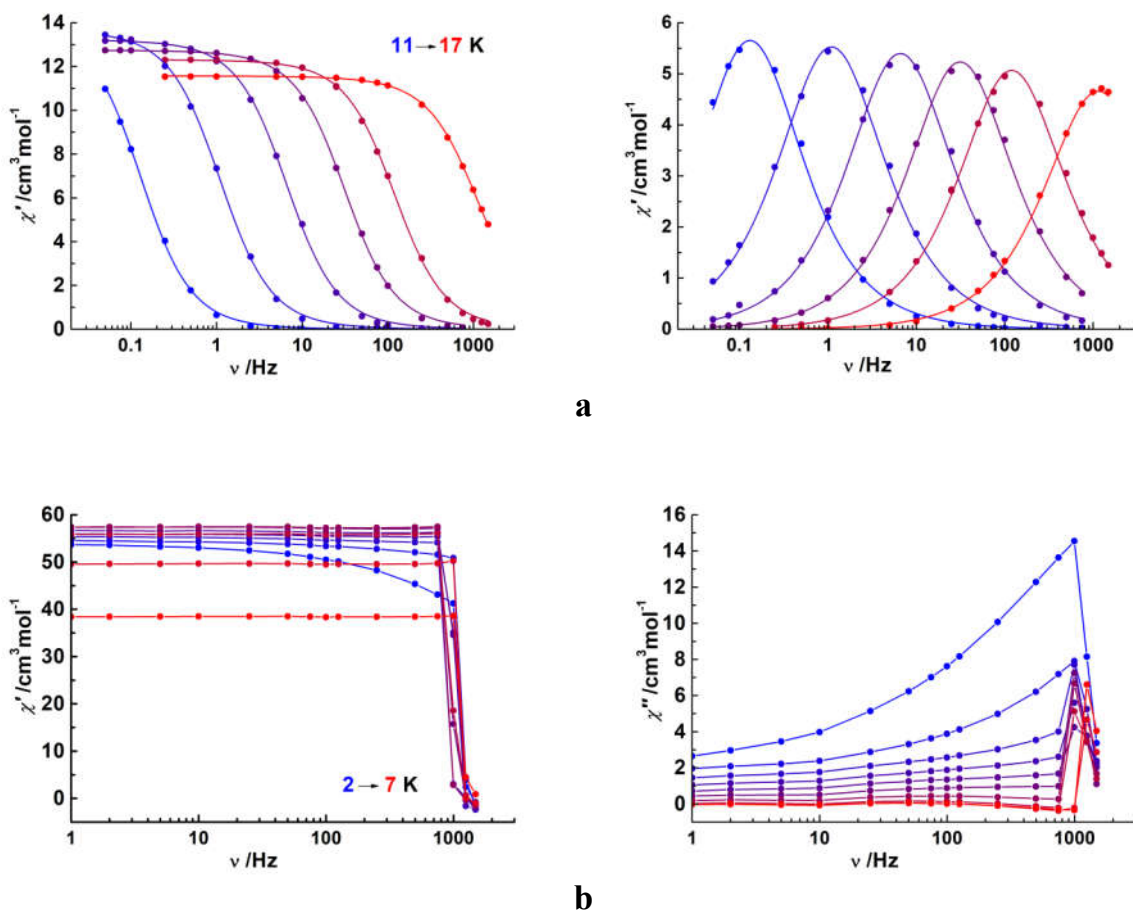
S10

Figure S9. Frequency dependencies of χ' (in-phase) and χ'' (out-of-phase) components of the AC magnetic susceptibility (under zero DC field with the ac field of 3.5 Oe and the frequency varies in range 0.01–1488 Hz) at different temperatures for $[Co(hfac)_2L]_n$ (a, the solid lines represent fitting using a single generalized Debye model) and $[Mn(hfac)_2L]_n$ (b, solid lines only guide).

Magnetic modeling

Experimental curve $\chi T(T)$ for [Co(hfac)$_2$L]$_n$ was fitted using the branch chain model with the following spin Hamiltonian:

$$\widehat{H} = \Sigma\{-2J\left[S_{Co,i(z)}\left(S_{R,i(z)} + S_{R,i-1(z)}\right)\right] + J_a L_{Co,i(z)} S_{Co,i(z)} + D L^2_{Co,i(z)} - \mu_B H(g_{Co} S_{Co,i(z)} +$$

$gRSR,iz+kLCo,iz)\},$

where J – intrachain exchange parameter; $g_R = 2$ (fixed), g_{Co} – g-factors of the radical and Co^{2+} ion; D – single-ion anisotropy parameter of Co^{2+} and k – orbital reduction factor.[5]

The fitting was performed using the following equation:

$$\chi T = \frac{N\mu_B^2}{k_B} \frac{[u^2 a + 2uc + \frac{(ua+c)^2}{b} + d]}{a + b}$$

$$a = [2e^z \cosh(3y) + 1]\cosh(6x) + [2e^z \cosh(y) + 1]\cosh(2x)$$

$$b = 2[e^z(\cosh(3y) + \cosh(y) + 1]$$

$$c = \{e^z[e^{-3y}(3v - k) + e^{3y}(3v + k)] + 3v\}\sinh(6x)$$
$$+ \{e^z[e^{-y}(v - k) + e^{-y}(v + k)] + v\}\sinh(2x)$$

$$d = \{e^z[e^{-3y}(3v - k)^2 + e^{3y}(3v + k)^2] + (3v)^2\}(1 + \cosh(6x)$$
$$+ \{e^z[e^{-y}(v - k)^2 + e^y(v + k)^2] + v^2\}(1 + cos\square(2x))$$

$$u = \frac{g_R}{2}; v = \frac{g_{Co}}{2}$$

$$x = \frac{J}{2k_B T}; y = \frac{-J_a}{2k_B T}; z = \frac{-D}{k_B T};$$

Frequency dependences of the in-phase (χ') and out-of-phase (χ'') AC magnetic susceptibilities were analyzed using the generalized Debye model:

$$\chi'(\omega) = \chi_S + (\chi_T - \chi_S)\frac{1 + (\omega\tau)^{1-\alpha}\sin\left(\frac{\pi\alpha}{2}\right)}{1 + 2(\omega\tau)^{1-\alpha}\sin\left(\frac{\pi\alpha}{2}\right) + (\omega\tau)^{2-2\alpha}}$$

$$\chi''(\omega) = \chi_T - \chi_S\frac{(\omega\tau)^{1-\alpha}\cos\left(\frac{\pi\alpha}{2}\right)}{1 + 2(\omega\tau)^{1-\alpha}\sin\left(\frac{\pi\alpha}{2}\right) + (\omega\tau)^{2-2\alpha}}$$

where χ_T – adiabatic susceptibility, χ_S – isothermal susceptibility, τ – relaxation time and α – parameter that describes width of a relaxation time distribution.
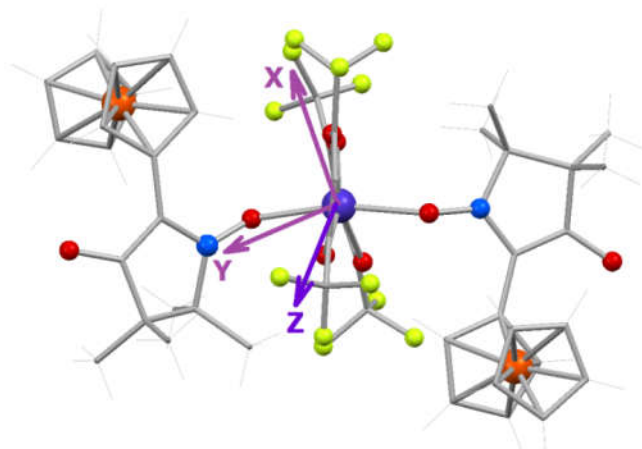
9. Quantum chemical calculations

Figure S10. Isolated L^d-Co-L^d fragment with two diamagnetic ligands L^d (Scheme 1S) being used to evaluate D-tensor by *ab initio* CASSCF quantum chemical calculations. Directions of the *D*-tensor main axes are shown by the corresponding arrows. The calculated values of the *D*-tensor are $D = -116$ cm^{-1} and $E/D = 0.21$.

Table 3 shows the energies of the six lower Kramers doublets for the L^d-Co-L^d complex, calculated using CASSCF(7.5). According to these calculations, the description of the magnetic properties of the L^d-Co-L^d complex up to temperatures T of about 250 K can be limited by two lower doublets (and then the *D*-tensor approximation can be used).

Table S3. Energies of the six lower Kramers doublets for the L^d-Co-L^d

Kramers doublet number	0	1	2	3	4	5
Kramers doublet energy / cm^{-1}	0.00	248	598	945	1794	1918

10. References

1   C. R. Groom, I. J. Bruno, M. P. Lightfoot and S. C. Ward, The Cambridge Structural Database, *Acta Crystallogr. Sect. B Struct. Sci. Cryst. Eng. Mater.*, 2016, **72**, 171–179.
2   R. A. A. Cassaro, S. G. Reis, T. S. Araujo, P. M. Lahti, M. A. Novak and M. G. F. Vaz, A Single-Chain Magnet with a Very High Blocking Temperature and a Strong Coercive Field, *Inorg. Chem.*, 2015, **54**, 9381–9383.
3   X. Y. Qin, G. Xiong, D. Liao, Y. Ma, P. Gao, X. L. Sun and P. Liu, Synthesis, crystal structure, and magnetism of [Mn(hfac)$_2$NIT(Ph-m-OPh)], *J. Coord. Chem.*, 2012, **65**, 2683–2691.
4   B. Sieklucka and D. Pinkowicz, *Molecular Magnetic Materials: Concepts and Applications*, John Wiley and Sons, Weinheim, Germany, 2017.
5   P. J. Van Koningsbruggen, O. Kahn, K. Nakatani, Y. Pei, J. P. Renard, M. Drillon and P. Legoll, Magnetism of A-copper(II) bimetallic chain compounds (A = iron, cobalt, nickel): one- and three-dimensional behaviors, *Inorg. Chem.*, 1990, **29**, 3325–3331.